



## Physical: Technical Report

## Ultrathin specimen preparation by a low-energy Ar-ion milling method

Masanori Mitome\*

International Center for Materials Nanoarchitectonics, National Institute for Materials Science,  
1-1 Namiki Tsukuba, Ibaraki 305-0044, Japan

\*To whom correspondence should be addressed. E-mail: mitome.masanori@nims.go.jp

**Abstract** The low-energy Ar-ion milling method was used to prepare ultrathin specimens for transmission electron microscope observation. The samples were thinned initially by a usual focused ion beam technique or typical Ar-ion milling with a high energy of 2–10 keV and were thinned additionally by an Ar-ion beam with an energy less than 1 keV, typically 500–900 eV. This low-energy ion beam was scanned over the specimen, and secondary electrons induced by the ion beam could be detected to form secondary electron images with a resolution of a few micrometre. Because a desired area can be selected and thinned by the low-energy ion beam, redeposition or cross contamination from irradiation of a metal grid that supports the sample can be prevented. It was shown that the low-energy Ar-ion beam thins a surface amorphous damage layer preferentially and effectively rather than a crystal specimen. Images from ultrathin specimens of two different materials revealed a detailed structure.

**Keywords** Ar-ion milling, sample preparation, ultrathin specimen, low-energy ion beam,  $\gamma$ -Ga<sub>2</sub>O<sub>3</sub>, (Zn, Cr)Te

**Received** 20 June 2012, accepted 12 October 2012

## Introduction

Ar-ion beam milling and focused ion beam (FIB) thinning are techniques that have been widely used to prepare specimens for transmission electron microscope (TEM) or scanning TEM (STEM) observations. It is well known that some amount of an amorphous damage layer is formed on the sample surface by the high-energy ion beam bombardment [1,2]. The damage layer causes background random noise on the TEM and STEM images, and the image contrast is often reduced.

A low-energy ion beam of a few kiloelectron volt can be used in FIB to reduce the damage [3,4], but the presence of damage still precludes high-resolution TEM or STEM observation. To remove the damage layer, some designs for low-energy ion

guns have been developed, and such guns have been applied to cleaning the sample surface [5,6].

The size of the low-energy ion beams used in the previous studies was about 350–1000  $\mu\text{m}$ , and the ion beam irradiates the specimen over a wide area, not only on the thin area preprocessed by the higher energy ion beam, but also on the non-milled thick areas or a metal grid that supports the sample. In these cases, the sample would be thinned by the low-energy ion beam, but redeposition and/or cross contamination is unavoidable.

A new ion gun design has recently become available that avoids the redeposition and the cross contamination. The new ion gun can converge a low-energy ion beam and scan the beam over the specimen. This study illustrates its application to

the preparation of TEM samples of an oxide material and a semiconductor.

## Methods

The low-energy Ar-ion milling apparatus used in this study was a Fischione Model 1040 NanoMill. An argon ion beam can be converged to less than  $2\ \mu\text{m}$  and scanned over a specimen. Secondary electrons induced by the ion beam are detected, and secondary electron images can be observed with a resolution of a few micrometres. A desired area can be selected and thinned by the low-energy Ar-ion beam.

Two kinds of specimen were thinned in this study. The first is a  $\gamma\text{-Ga}_2\text{O}_3$  layer grown on an MgO substrate by the vapor-phase transport method [7]. Only the  $\beta$  form of  $\text{Ga}_2\text{O}_3$  is stable; the metastable  $\gamma$  form has attracted great interest recently because it shows emission of visible blue–green light [8,9] and room temperature ferromagnetism by Mn doping [10]. A small lamella was picked up by a FIB Hitachi FB-2000A and fixed on a side wall of a post on an Omniprobe grid, as shown in Fig. 1a, to prevent redeposition or cross contamination in the following low-energy Ar-ion milling process. The

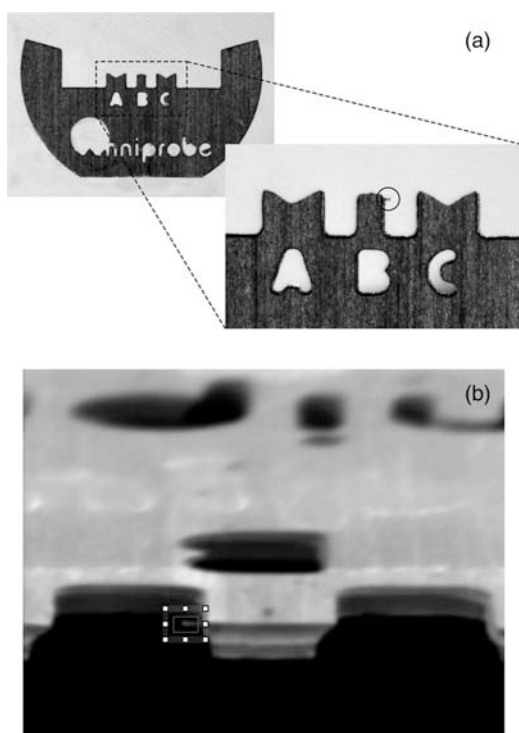


**Fig. 1.** A sample lamella was fixed on a side wall of a post on an Omniprobe grid (a). A secondary electron image induced by the low-energy Ar-ion beam (b).

lamella was thinned initially up to less than  $350\ \text{nm}$  in thickness by the FIB with a  $30\ \text{kV}$  Ga ion beam and thinned additionally by the low-energy Ar-ion beam at a small glancing angle. The area to be thinned was selected from the secondary electron image shown in Fig. 1b. The thinning process was performed several times with a short exposure time of about  $10\text{--}30\ \text{min}$  for each side.

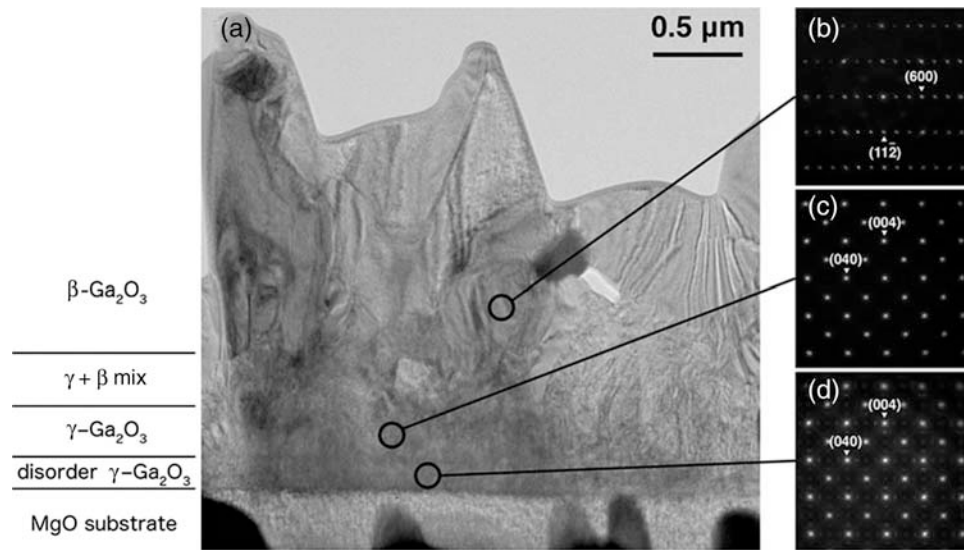
The second specimen was a high-temperature ferromagnetic semiconductor (Zn, Cr)Te film that was grown on a GaAs substrate by molecular beam epitaxy [11]. It has been suggested that Cr-rich nanoparticles are formed in the film and dominate the ferromagnetism. Observation of the chromium distribution in the film is important to the clarification of the origin of the ferromagnetism. The sample was thinned initially by a JEOL EM-09100IS Ion Slicer with a  $2\text{--}8\ \text{keV}$  Ar-ion beam and thinned additionally by the low-energy ion beam.

The TEM used in this study is a JEM-3100FEF with a  $300\text{-kV}$  acceleration voltage [12]. An omega-type in-column energy filter is equipped to take elemental distribution images, and an inelastic scattered electrons contribution has been removed from all the images shown in this paper by the energy filter. Image quality and damage layer thickness were investigated after each thinning process for both specimens.

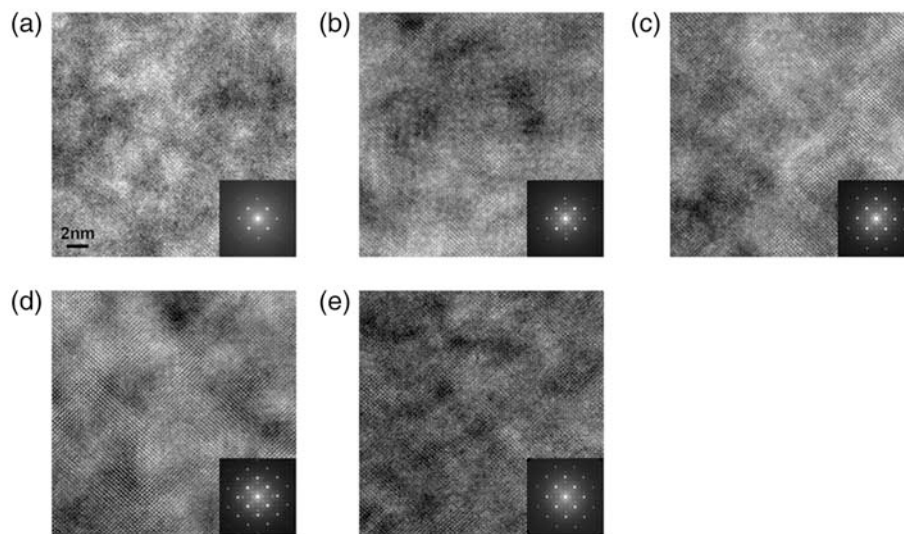
## Results

Figure 2a shows a TEM image of the  $\text{Ga}_2\text{O}_3$  film after initial thinning by FIB. Some diffraction patterns taken from small selected areas shown by circles are displayed in Fig. 2b–d. While the diffraction pattern in Fig. 2b can be assigned to  $\beta\text{-Ga}_2\text{O}_3$  with a monoclinic crystal form, Fig. 2c and 2d is assigned to  $\gamma\text{-Ga}_2\text{O}_3$  with a cubic crystal form. Since some forbidden reflection spots are seen in Fig. 2d, it has been suggested that the interfacial layer near the MgO substrate includes some defects such as twins or stacking faults [7].

Figure 3a shows a higher magnification image of the disordered  $\gamma\text{-Ga}_2\text{O}_3$  interfacial layer, and the inset shows the diffractogram. The weak forbidden reflection spots are barely seen in the diffuse intensity caused by the amorphous damage layer. The initial sample thickness was estimated as  $320\ \text{nm}$  by



**Fig. 2.** A TEM image of a  $\text{Ga}_2\text{O}_3$  film that was thinned by FIB (a). Selected area electron diffraction patterns (b)–(d) that were taken from the circled areas in (a).



**Fig. 3.** TEM images of a disordered  $\gamma\text{-Ga}_2\text{O}_3$  layer. Directly after the FIB thinning process (a), after a first low-energy Ar-ion milling (b). (c)–(e) TEM images after further milling processes. The insets show the associated diffractograms.

a Kramers–Kronig analysis of an electron energy loss spectrum (EELS).

Both the top and the bottom surfaces of the sample were thinned additionally by a 900 eV ion beam for 60 min each at a glancing angle of  $10^\circ$ . The TEM image after the additional thinning process is shown in Fig. 3b, with the associated diffractogram. The forbidden reflection spots are seen in the diffractogram. The sample thickness was estimated as 145 nm. The sample itself was thinned,

and moreover, the amorphous damage layer was reduced significantly.

The sample was thinned several times using a 500-eV ion beam. The TEM images after each thinning process are shown in Fig. 3c–e with the diffractograms. The thicknesses estimated by EELS are 100, 60 and 25 nm, respectively. The diffuse intensity caused by the amorphous layer is reduced gradually, and the diffraction spots from a crystal layer are seen more clearly.

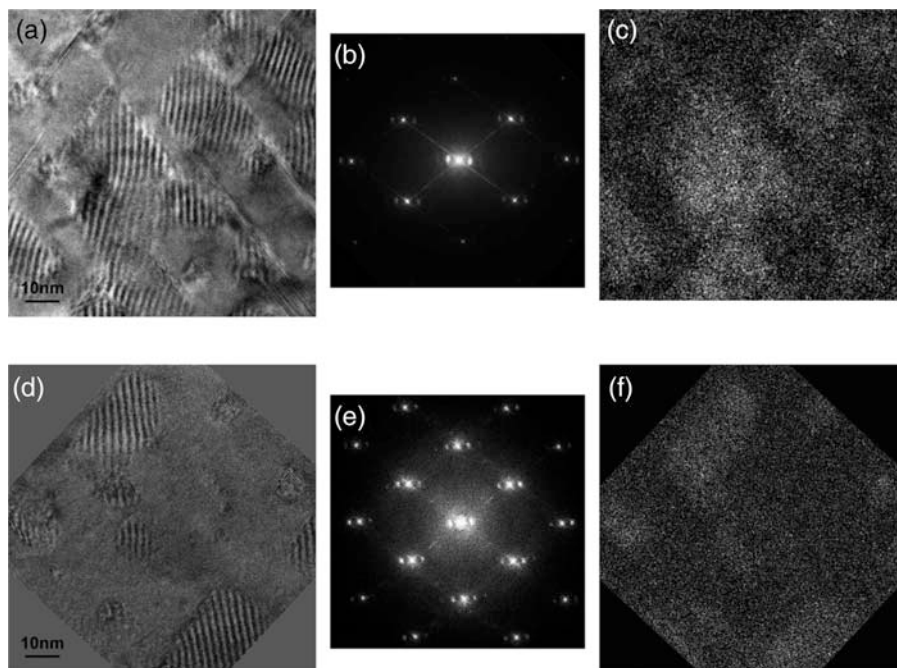


**Fig. 4.** TEM images (a), (d), diffractograms (b), (e) and chromium maps (c), (f) of the ferromagnetic semiconductor (Zn, Cr)Te. (a)–(c) a specimen directly after the usual Ar-ion milling with the high-energy ion beam. (d)–(f) a specimen after the low-energy Ar-ion milling.

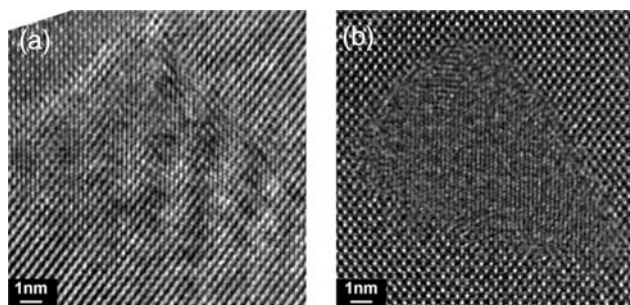


**Fig. 5.** High-magnification TEM images of a chromium-rich grain in the ferromagnetic semiconductor. (a) a specimen directly after the usual Ar-ion milling with the high-energy ion beam, and (b) a specimen after the low-energy Ar-ion milling.

Figure 4 shows results for the high-temperature ferromagnetic semiconductor (Zn, Cr)Te. Figure 4a–c shows a TEM image, a diffractogram and a chromium map image for the sample after the initial thinning by the Ion Slicer with a 2–8 keV Ar-ion beam. Chromium-rich grains were formed in a matrix of ZnCr crystal. The grains have a lattice constant different from that of the matrix, and thus, some Moiré fringes can be seen in Fig. 4a and in the higher magnification image in Fig. 5a. The sample was already thinned in this way down to 30 nm, but the grains overlapped one another because their size is 10–30 nm. To clarify the crystal

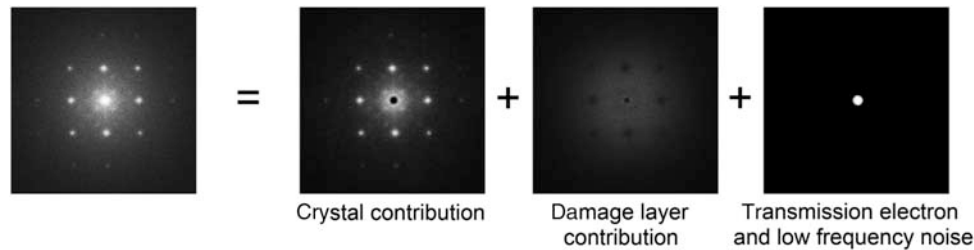
structure of the grains, the specimen should be thinned further.

Figure 4d–f shows a TEM image, a diffractogram and a chromium map image for the specimen after further milling with a 500-eV Ar-ion beam. The sample thickness is now less than 10 nm, and thus, every grain is separated from one another in Fig. 4d. Moiré fringes are still seen in Fig. 4d, but some small grains, such as that in Fig. 5b, show no Moiré fringes. The top and the bottom of the grain were trimmed without overlapping of the matrix ZnTe. The lattice images were investigated, and it was concluded that the grains consist of hexagonal CrTe nanocrystals [13].

## Discussion

The total thickness of the specimen can be measured from EELS analysis, but the partial thicknesses of the crystal layer and the amorphous damage layer are unknown. A Wiener filter was used to separate the contributions of the damage layer and the crystal layer. The Wiener filter is a noise-reduction filter widely used in various fields, and it can separate a signal from a background noise.

The following process was performed for diffractograms in Fig. 3: (i) divide the Fourier components into a sharp signal and a broad background by a local two-dimensional Wiener filter [14], (ii) subtract the intensity around a center spot from the sharp signal by a high-pass filter to remove a transmission electron contribution and a low-frequency noise and (iii) evaluate a ratio between intensity sums for the sharp signal without the center spot and the broad background. Every diffractogram can be separated into three contributions as shown in Fig. 6. The sharp signal and the broad background can be assigned to a crystal layer contribution and an amorphous damage layer contribution, respectively. A contribution from inelastic scattered electrons might be merged into the broad background. However, all images are zero-loss images taken by the energy filter, and thus, the broad background can be interpreted as the pure contribution from the amorphous damage layer.



**Fig. 6.** A diffractogram separates into three contributions: a crystal contribution, a damage layer contribution and a transmission electron contribution with a low-frequency noise. A Wiener filter is used to extract the crystal contribution from the background caused by the damage layer.

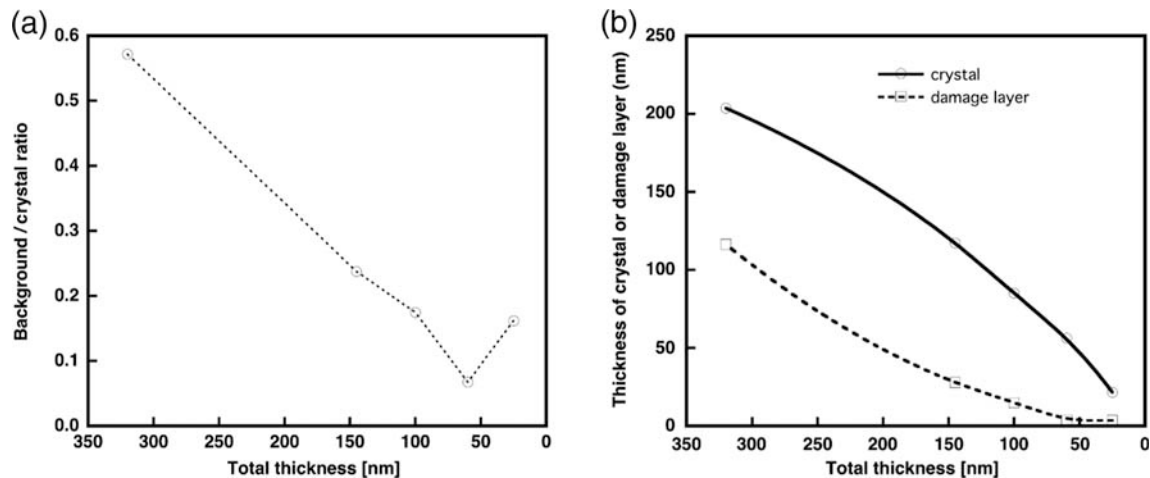


**Fig. 7.** A ratio of a background to a crystal contribution (a). Total thicknesses were measured by an EELS analysis. Partial thicknesses of a crystal layer and an amorphous damage layer (b). Curves are guides to the eye only.

The TEM images in Fig. 3 were taken with different intensities of the incidence electron, and therefore, the absolute thickness of the crystal layer and the damage layer cannot be estimated from the process mentioned above. However, the ratio between the crystal layer and the amorphous damage layer can be estimated for each image. Since the total absolute thickness can be measured from EELS analysis, the partial thickness for the crystal layer and the amorphous damage layer can be evaluated from the total thickness and the ratio.

The ratio of the background contribution to the crystal contribution (b/c ratio) is shown in Fig. 7a. It decreased monotonously up to a total thickness of 60 nm, but it increased at a total thickness of 25 nm. The partial thicknesses of the crystal layer and the amorphous damage layer are evaluated from the b/c ratio and the total thickness as shown in Fig. 7b. A curve for the crystal layer thickness is convex upward, whereas a curve for the damage

layer is convex downward. The damage layer was thinned primarily rather than the crystal layer. The minimum thickness of the damage layer was 4 nm at the total thickness of 60 nm. At the total thickness of 25 nm, the damage layer remained 4 nm as before, but the crystal was thinned up to 20 nm. Consequently, the b/c ratio increases at the total thickness of 25 nm. These results show that the low-energy Ar-ion beam thins the surface amorphous layer preferentially and effectively rather than the crystal layer.

The typical ion beam current was 120 pA, and the scanned area for the thinning process was usually selected to be about  $10 \times 10 \mu\text{m}$ . The beam current was quite small, but the ion beam was converged to  $2 \mu\text{m}$  and so the beam density was high enough to achieve a practical milling rate. The milling rate was roughly estimated as  $0.7 \text{ nm min}^{-1}$  for oxide materials and semiconductors under these conditions, although it depends on the materials and the thinning area.

In this study, the results using an Ar-ion beam energy of 500 eV or 900 eV were described. An energy as low as 100 eV has also been investigated, but the thinning rate was extremely reduced for both oxide and semiconductor materials. It appears that 500–900 eV is appropriate for these inorganic materials. As yet, we have no data for metals or organic materials, but it can be supposed that the lower energy is better for these materials.

### Concluding remarks

We have reported the results of sample preparation using the low-energy Ar-ion milling method. The low-energy Ar-ion beam can thin the amorphous damage layer preferentially and effectively rather than the crystal specimen, and the damage layer was substantially reduced up to 4 nm. The structure can be investigated in detail with the ultrathin specimen with the less damage layer, and the crystal structure of some small grains can be revealed.

The ion beam was converged to  $2 \mu\text{m}$  and scanned over the specimen. The desired thinning area can be selected from the secondary electron

image. The ion beam density is high enough to thin the specimen within 1 h. This low-energy Ar-ion milling method is appropriate for post processing of an FIB or a usual Ar-ion milling method with a high-energy ion beam.

### Acknowledgements

The author acknowledges Prof. Shigemi Kohiki, Kyusyu Institute of Technology, for providing the sample of  $\gamma\text{-Ga}_2\text{O}_3$  and also thanks Prof. Shinji Kuroda and Dr Ken Kanazawa, Tsukuba University, for preparing the sample of  $(\text{Zn}, \text{Cr})\text{Te}$  and for discussion on the crystal structure. The author also acknowledges discussion with Dr Kazuo Ishizuka on the image processing using the Wiener filter.

### References

- Schuhrike T, Mändl M, Zweck J, and Hoffmann H (1992) Investigation of surface amorphization of silicon wafers during ion-milling. *Ultramicroscopy* **41**: 429–433.
- Barna A, Pecz B, and Menyhard M (1999) TEM sample preparation by ion milling amorphization. *Micron* **30**: 267–276.
- Kato N I (2004) Reducing focused ion beam damage to transmission electron microscopy samples. *J. Electron Microsc.* **53**: 451–458.
- Schaffer M, Schaffer B, and Ramasse Q (2012) Sample preparation for atomic-resolution STEM at low voltages by FIB. *Ultramicroscopy*. **114**: 62–71.
- Scott J, Docherty T, MacKenzie M, Smith W, Miller B, Collins L, and Craven J (2006) Sample preparation for nanoanalytical electron microscopy using the FIB lift-out method and low energy ion milling. *J. Phys. Conf. Ser.* **26**: 223–226.
- Suess MJ, Mueller E, and Wepf R (2011) Minimization of amorphous layer in  $\text{Ar}^+$  ion milling for UHR-EM. *Ultramicroscopy* **111**: 1224–1232.
- Mitome M, Kohiki S, Hori K, Fukuta M, and Bando Y (2006) Epitaxial growth of  $\beta\text{-Ga}_2\text{O}_3$  nanocolumns on MgO substrate. *J. Cryst. Growth* **286**: 240–246.
- Chen T and Tang K (2007)  $\gamma\text{-Ga}_2\text{O}_3$  quantum dots with visible blue-green light emission property. *Appl. Phys. Lett.* **90**: 053104.
- Wang T, Farvid S S, Abulikemu M, and Radovanovic P V (2010) Size-tunable phosphorescence in colloidal metastable  $\gamma\text{-Ga}_2\text{O}_3$  nanocrystals. *J. Am. Chem. Soc.* **132**: 9250–9252.
- Hayashi H, Huang R, Ikeno H, Oba F, Yoshioka S, Tanaka I, and Sonoda S (2006) Room temperature ferromagnetism in Mn-doped  $\gamma\text{-Ga}_2\text{O}_3$  with spinel structure. *Appl. Phys. Lett.* **89**: 181903.
- Kuroda S, Nishizawa N, Takita K, Mitome M, Bando Y, Osuch K, and Dietl T (2007) Origin and control of high-temperature ferromagnetism in semiconductors. *Nat. Mater.* **6**: 440–446.
- Mitome M, Bando Y, Golberg D, Kurashima K, Okura Y, Kaneyama T, Naruse M, and Honda Y (2004) Nanoanalysis by a high-resolution energy filtering transmission electron microscope. *Microsc. Res. Techniq.* **63**: 140–148.
- Kobayashi H, Nishio Y, Kanazawa K, Kuroda S, Mitome M, and Bando Y (2012) Structural analysis of the phase separation in magnetic semiconductor  $(\text{Zn}, \text{Cr})\text{Te}$ . *Phys. B* **407**: 2947–9.
- Eilers P H C, Ishizuka K, IMC16, Sapporo (2006) 964. A plug-in software “HREM Filters Pro” is released from HREM Research Inc.